Atomic-scale observations of electrical and mechanical manipulation of topological polar flux closure

Xiaomei Li[a,b,c,1], Congbing Tan[d,e,1], Chang Liu[f,1], Peng Gao[b,g,h,2], Yuanwei Sun[b,h], Pan Chen[a,c], Mingqiang Li[b,h], Lei Liao[a,c], Ruixue Zhu[b,h], Jinbin Wang[e], Yanchong Zhao[a,c], Lifen Wang[a], Zhi Xu[a,c,i], Kaihui Liu[g,j], Xiangli Zhong[e,2], Jie Wang[f,k,2], and Xuedong Bai[a,c,i,2]

[a]Beijing National Laboratory for Condensed Matter Physics, Institute of Physics, Chinese Academy of Sciences, 100190 Beijing, China; [b]International Center for Quantum Materials, School of Physics, Peking University, 100871 Beijing, China; [c]School of Physical Sciences, University of Chinese Academy of Sciences, 100049 Beijing, China; [d]Department of Physics and Electronic Science, Hunan University of Science and Technology, 411201 Xiangtan, China; [e]School of Materials Science and Engineering, Xiangtan University, 411105 Xiangtan, China; [f]Department of Engineering Mechanics, Zhejiang University, 310027 Hangzhou, China; [g]Collaborative Innovation Centre of Quantum Matter, 100871 Beijing, China; [h]Electron Microscopy Laboratory, Peking University, Beijing 100871, China; [i]Songshan Lake Materials Laboratory, 523808 Dongguan, China; [j]State Key Laboratory for Artificial Microstructure and Mesoscopic Physics, School of Physics, Peking University, 100871 Beijing, China; and [k]Key Laboratory of Soft Machines and Smart Devices of Zhejiang Province, Zhejiang University, 310027 Hangzhou, China

Edited by S.-W. Cheong, Rutgers University, Piscataway, NJ, and accepted by Editorial Board Member Zachary Fisk June 22, 2020 (received for review April 16, 2020)

The ability to controllably manipulate complex topological polar configurations such as polar flux-closures via external stimuli may allow the construction of new electromechanical and nanoelectronic devices. Here, using atomically resolved in situ scanning transmission electron microscopy, we find that the polar flux-closures in $PbTiO_3/SrTiO_3$ superlattice films are mobile and can be reversibly switched to ordinary single ferroelectric *c* or *a* domains under an applied electric field or stress. Specifically, the electric field initially drives movement of a flux-closure via domain wall motion and then breaks it to form intermediate *a*/*c* striped domains, whereas mechanical stress first squeezes the core of a flux-closure toward the interface and then form *a*/*c* domains with disappearance of the core. After removal of the external stimulus, the flux-closure structure spontaneously recovers. These observations can be precisely reproduced by phase field simulations, which also reveal the evolutions of the competing energies during phase transitions. Such reversible switching between flux-closures and ordinary ferroelectric states provides a foundation for potential electromechanical and nanoelectronic applications.

ferroelectric | flux-closure domains | manipulation | atomic resolution | in situ (S)TEM

Topological structures in ferromagnetic materials (e.g., skyrmions) have shown great potential for application to electromechanical devices (1), spintronic information storage devices (2, 3) and logic devices (4–6) owing to their topologically protected states (7). Given the similarities between ferroelectricity and ferromagnetism, the complex low-dimensional topological polar structures that are inherent to ferroelectric materials, such as quadrant domains (8), polar flux-closures (9, 10), and vortices (11, 12), have also been attracting increasing attentions in recent years (1, 9, 10, 12–16). A polar flux-closure is a stable topological domain structure formed mainly by the interplay between a depolarization field and mechanical boundary conditions (1, 17–21) and consisting of short segmented 90° and 180° domain walls (9, 22). The small size of flux-closure arrays, with their high density of small segmented domain walls and large strain gradients in the vicinity of the core, mean that these structures have great potential for application to nanoscale ferroelectric devices (9).

Most applications of ferroelectric materials require an ability to manipulate polar states through external stimuli. Given that flux-closures are formed as a result of a delicate balance between electrostatic and strain boundary conditions (1, 17–21), phase transitions from the topological configuration to other polar states are expected to occur under the action of external stimuli that can disrupt this balance. In fact, for other types of topological polar structure vortices, theoretical investigations have predicted that the vortex structure can be converted to ordinary ferroelectric phases under driving by temperature, electric field, or stress (14, 19, 23, 24). For instance, a transformation from a vortex structure to an ordinary ferroelectric phase has been predicted in $Pb(Zr_{0.5}Ti_{0.5})O_3$ nanoparticles to accommodate a homogeneous electric field (13). On the other hand, experimental investigations have successfully demonstrated transitions of domain topology at the mesoscale by cooling through the Curie temperature (25, 26) or applying an electric field with piezoresponse force microscopy (PFM) (13, 27–29). However, the phase transition behavior of flux-closures has rarely been studied either theoretically or experimentally. Unlike a vortex, which consists of continuously rotated electric dipoles without any domain walls, a polar flux-closure contains multiple short segmented 90° and 180° domain walls with mutual interactions. Thus, the switching behavior of a flux-closure is likely to be very

Significance

Flux-closures, stable topological polar structures of nanometer size, are considered to be promising candidates as elements of future nanoelectronic and electromechanical devices. Understanding their phase transition pathways under external stimuli is therefore of vital importance for these potential applications. Here, using an atomically resolved *in situ* electron microscopy technique, we track the evolutions of the polarization of the flux-closure structure under both electric and stress fields with atomic resolution. We find that the flux-closure can be reversibly and controllably manipulated between the topological and ordinary ferroelectric states, enabling potential applications in electromechanical and nanoelectronic devices.

Author contributions: C.T., P.G., and X.B. designed research; X.L., C.T., C.L., Y.S., P.C., M.L., L.L., Jinbin Wang, X.Z., and Jie Wang performed research; Z.X. contributed new reagents/analytic tools; X.L. and P.G. analyzed data; C.T., C.L.,Y.S., R.Z., Y.Z., L.W., K.L., Jie Wang, and X.B. assisted with data analysis; and X.L., R.Z., and P.G. wrote the paper with contributions from C.T., C.L., Jie Wang, and X.B.

The authors declare no competing interest.

This article is a PNAS Direct Submission. S.-W.C. is a guest editor invited by the Editorial Board.

[1]X.L., C.T., and C.L. contributed equally to this work.

[2]To whom correspondence may be addressed. Email: p-gao@pku.edu.cn, xlzhong@xtu.edu.cn, jw@zju.edu.cn, or xdbai@iphy.ac.cn.

This article contains supporting information online at https://www.pnas.org/lookup/suppl/doi:10.1073/pnas.2007248117/-/DCSupplemental.

First published July 24, 2020.

different from that of a vortex. On the other hand, surface probe-based PFM is usually limited in its spatial resolution and does not have the capability to obtain full information regarding nanosized polar topological structures, which have highly structured inhomogeneities and strong charge–lattice coupling, hidden within thin films. By contrast, recent advances in atomically resolved in situ scanning transmission electron microscopy (STEM) have presented the possibility of capturing structural evolutions of individual polar vortices (30, 31). Therefore, in the present study we utilize this cutting-edge technique to investigate whether or not topological polar flux-closures can be controllably switched to ordinary ferroelectric domains, and we further reveal the detailed transition behavior and underlying mechanism by combining this experimental investigation with phase field simulations.

Here we experimentally demonstrate that under external stimuli, topological flux-closures in $PbTiO_3/SrTiO_3$ (PTO/STO) superlattice films are mobile and switchable. Under an electric field, a flux-closure first transforms into an intermediate *a*/*c* striped domain by lateral movement of its core and by breaking of its structure, and this eventually leads to the formation of a single *c* domain. Under compressive stress, a flux-closure first transforms into an *a*/*c* domain, which is accompanied by shrinkage of the *c* domain and disappearance of the flux-closure core, before final transformation into a single *a* domain. Phase field simulations reveal the evolution of the competing energies during these phase transitions. In both cases, the flux-closure returns to its original state when the external stimulus is removed. In other words, a flux-closure as a topological structure can be reversibly broken and recovered by application of either an electric field or a compressive strain. It is this ability of flux-closures to reversibly switch to ordinary ferroelectric domain structures that makes them potential candidates for application to nanoelectronics and electromechanical devices.

Results

A dark-field transmission electron microscopy (TEM) image (Fig. 1*A*) shows the morphology of a $[(PTO)_{19}/(STO)_{11}]_8$ film grown on $GdScO_3$ (110) [$(001)_{pc}$, where pc indicates pseudocubic indices] substrate with an $SrRuO_3$ buffered layer by pulse laser deposition (growth details are provided in *Methods*), where the subscripts "19" and "11" correspond to the thicknesses of the PTO and STO layers in unit cells, and "8" denotes eight periods of the $(PTO)_{19}/(STO)_{11}$ unit. In this dark-field image, the STO layers show bright and uniform contrast, while the PTO layers exhibit a two-dimensional (2D) periodic sinusoidal array with dark contrast corresponding to the *c* domain (with the *c* axis along the out-of-plane direction), whereas the domains with triangular configurations give rise to another periodic array with bright contrast corresponding to the *a* domain (with the *c* axis along the in-plane direction) (9). This morphology is identical to that previously reported for the alternate clockwise and counterclockwise flux-closure quadrants (9, 10). A high-angle annular

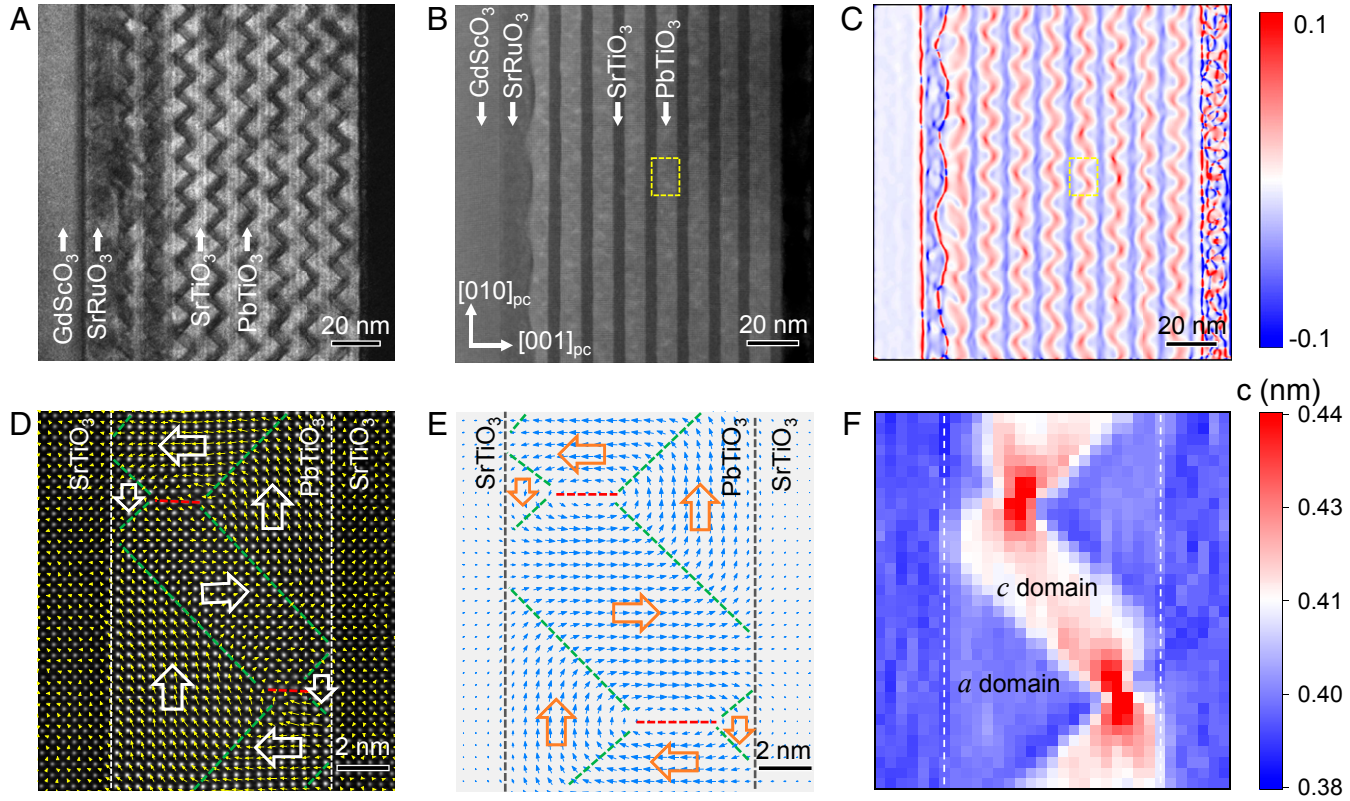

Fig. 1. Characterization of flux-closures in PTO/STO superlattices. (*A*) Cross-sectional dark-field TEM image of a PTO/STO superlattice formed by reflection with $\boldsymbol{g} = 200$, showing the alternative arrangement of STO and PTO on a GSO substrate. Flux-closure domains in the PTO layer show wave-like features. (*B*) Atomically resolved HAADF-STEM image showing a sharp interface between PTO and STO layers. (*C*) Corresponding GPA analysis showing the distribution of out-of-plane strain ε_{yy}. The wave-like features can be captured by GPA. (*D*) Enlarged view of HAADF-STEM image overlaid with polar vectors showing the flux-closure polar pattern in the PTO layer, while no substantial displacements exist in the reference cubic STO layer. The green and red dashed lines indicate the 90° and 180° domain walls, respectively. White arrows denote the polarization direction of PTO, forming alternate clockwise and counterclockwise flux-closures. (*E*) Flux-closure domain pattern predicted from phase field simulation, which shows good agreement with the experimental data. The polarizations are represented by blue arrows, with the 90° and 180° domain walls denoted by green and red dashed lines, respectively. (*F*) Out-of-plane lattice constant mapping corresponding to the image in *D*, showing the distribution of *a* and *c* domains in the PTO layer, analogous to GPA. The white dashed lines label the interface between PTO and STO.

dark field (HAADF) scanning TEM (STEM) image (Fig. 1*B*) shows a sharp interface between PTO and STO, while slight variation of the contrast is due to the presence of domain walls. The domain structure can be mapped using geometric phase analysis (GPA) (32, 33). The red periodic wave-like structure corresponding to larger out-of-plane lattice constant, as shown in Fig. 1*C*, represents the *c* domains, while the remaining blue-colored area denotes *a* domains in the PTO layers, and the STO layer is uniformly dark blue owing to the smaller out-of-plane lattice constant, which is consistent with the contrast in the dark-field image. Therefore, both dark-field and the atomically resolved STEM images can be utilized to monitor the evolution of flux-closure structures under external stimuli. The former has better temporal resolution, while the latter has better spatial resolution. The combination of the two imaging modes enables us to capture all the details during phase transitions down to the atomic scale.

A typical magnified area (outlined by the yellow frame in Fig. 1 *B* and *C*) of the atomically resolved HAADF-STEM images overlaid with displacement vectors in Fig. 1*D* represents the spontaneous polarization, the direction of which is opposite to the displacement direction of Ti atoms respective to the neighboring Pb atoms (as shown in detail in *SI Appendix*, Fig. S1) (34, 35). There is a typical clockwise and counterclockwise flux-closure pair pattern shown in Fig. 1*D*, while there are negligibly tiny displacement vectors in the reference STO layer. The phase field simulation in Fig. 1*E* shows good agreement with the experimental observations. The adjacent *c* domains with opposite polarization directions give rise to a short 180° domain wall, at the bottom of which the small *a* domain is the product of a strong depolarization field. The formation of a large *a* domain is mainly to balance the large tensile strain (22), corresponding to the triangular regions with bright contrast in the dark-field TEM images (Fig. 1*A*) and the triangular regions in blue in the GPA (Fig. 1*C*). The out-of-plane lattice constant mapping (Fig. 1*F*) corresponding to Fig. 1*D*, which was obtained by a 2D Gaussian algorithm (35, 36) from Fig. 1*D*, also gives rise to a sinusoidal feature of the flux-closure analogous to GPA result, indicating that the flux-closure is closely associated with the out-of-plane lattice constant, which enables us effectively distinguish the domain structure of the flux-closure.

To investigate the structural evolution, this cross-sectional superlattice film was then subjected to in situ electrical and mechanical stimuli via a scanning tungsten probe or indentor in a TEM with various image and diffraction modes. Electric fields were mainly applied along the out-of-plane direction, providing a driving force for the growth of the *c* domains, as shown in Fig. 2*A*. The GPA images (Fig. 2 *B*–*F*) corresponding to a typical chronological HAADF-STEM image series (*SI Appendix*, Fig. S2) show that the phase transition starts under the tip (the eighth layer, marked in Fig. 2*A*) at +5 V, as the contrast in GPA becomes uniform red, which is a feature of the *c* domain. The second layer transforms into tilted stripes, corresponding to *a*/*c* domains, at +7 V. With increasing voltage, more layers show *c* domain characteristics, indicating a transformation from the flux-closure to the *c* domain, with an intermediate *a*/*c* domain mixture.

To clearly display the evolution process for each flux-closure, three typical regions outlined in yellow, orange, and green in Fig. 2*A* are enlarged in Fig. 2 *G*–*I*. The specific evolution from the flux-closure to the *a*/*c* domain is indicated by the black ellipse in Fig. 2*G*, in which the *c* domain with upward polarization (pointing to the right in the image, c^+) gradually shrinks via motion of 90° and 180° domain walls as well as the flux-closure core and eventually disappears. Another region in Fig. 2*H* shows that the *a* domain is gradually converted into a *c* domain with downward polarization (pointing to the left, c^-). The inhomogeneous switching is likely related to the inhomogeneous distribution of electric fields due to the tip-shape electrodes (for details, see *Methods*; results are displayed in *SI Appendix*, Fig. S3). Near the tip at the top surface with larger field strength in Fig. 2*I*, a large c^- domain is generated. Furthermore, from the finite-element simulated field distribution in *SI Appendix*, Fig. S3, the critical electric field strength to initiate the transition from the flux-closure to the *a*/*c* domain is estimated to be ~40 MV/m, which is in reasonable agreement with the phase field simulated value ~23.7 MV/m. The discrepancy is likely due to the contact resistance causing some of the voltage drop in the experiments. Under a negative voltage, the dark-field images show the same phenomenon (*SI Appendix*, Fig. S4), indicating that the flux-closure can be controllably switched to c^+ (upward) and c^- (downward) via application of an electric field.

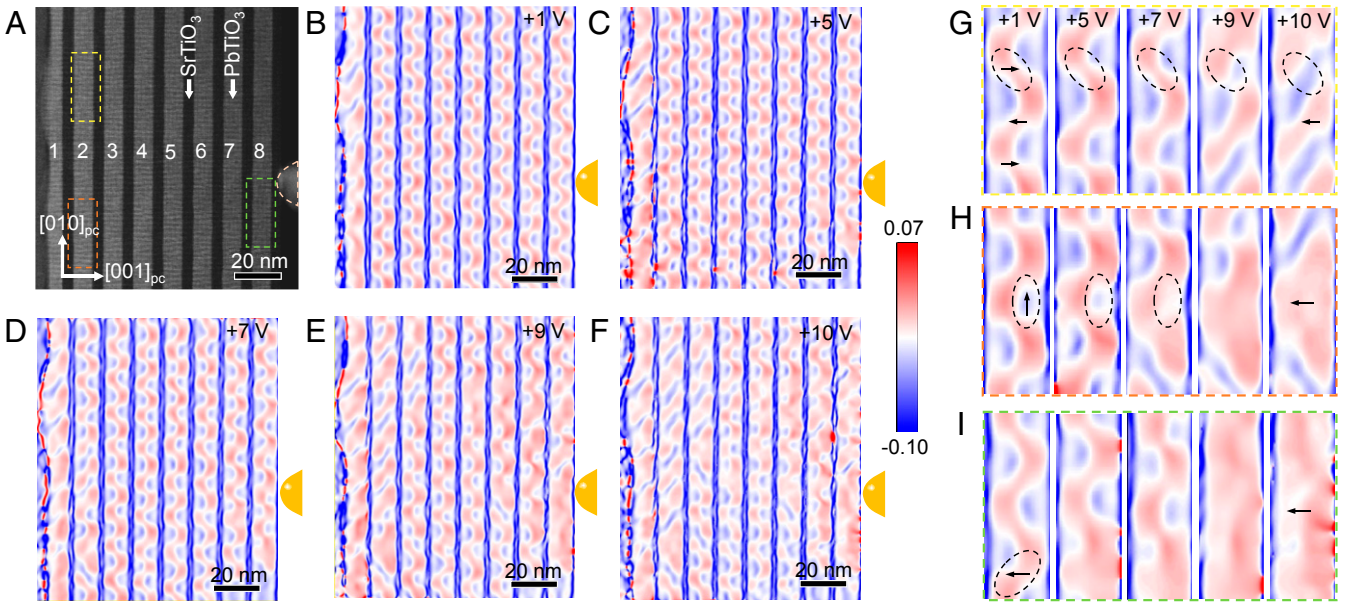

Fig. 2. Tracking the transition process of a flux-closure under increasing electrical field at the atomic scale. (*A*) HAADF-STEM image before application of an electric field. (*B*–*F*) Out-of-plane strain (ε_{yy}) maps extracted from the GPA corresponding to a sequence of HAADF-STEM images acquired in time series under different electric fields, showing the evolution of the domain pattern. (*G*–*I*) Enlarged GPA images of the representative areas outlined by yellow, orange, and green rectangles in *A* extracted from *B*–*F*. Thin black arrows indicate the polarization direction of PTO.

The transition is reversible. Removal of the electric field leads to spontaneous recovery from the *c* domain to the flux-closure state. In Fig. 3*A*, the atomically resolved HAADF images of the tilted stripes taken at + 9 V show an alternating array of *a*/*c* domains, and their presence is confirmed by the corresponding out-of-plane lattice constant mapping shown in Fig. 3*B*. As the voltage decreases, a representative region, outlined by the black ellipse, displays evolution from an *a*/*c* domain to a flux-closure; that is, a red-colored *c* domain appears in the originally blue-colored *a* domain and gradually becomes larger until it joins with an adjacent *c* domain, resulting in its transformation into a flux-closure structure (Fig. 3*B*). Note that the new c^+ domain nucleates at the corner of an *a* domain, a c^- domain, and a PTO/STO interface (the left interface in the image, outlined by the black ellipse in Fig. 3*B*), because an interface with discontinuous electric dipoles always has a lower nucleation barrier for polarization switching. Thus, a new flux-closure is formed, accompanied by nucleation of a c^+ domain. Once the c^+ domain reaches the other interface (the right one in the image), another flux-closure is generated.

Flux-closures can also be manipulated by a stress field. Application of a compressive force along the film, as shown in Fig. 4*A*, typically favors in-plane polarization, leading to the growth of a large *a* domain. This process is shown chronologically in Fig. 4 *B*–*G* through the GPA corresponding to the chronological HAADF-STEM images (*SI Appendix*, Fig. S5). The compressive stress was controlled to gradually increase from Fig. 4 *B*–*F* and then gradually decrease from Fig. 4 *F*–*G*. The flux-closure transition driven by mechanical stress begins at the region in contact with the tip with relatively large strength. As the applied mechanical force increases, the transformed region expands further toward the substrate, and more flux-closures are converted into *a* domains. The enlarged images in Fig. 4 *H* and *I* show that the *c* domains (red stripes) gradually shrink, while the large *a* domains (blue regions) expand. The large *a* domains become larger and larger, and this is accompanied by movement of two 90° domain walls on both sides to the *c* domain and shortening of the 180° domain wall, which simultaneously causes the flux-closure core to move along the 180° domain wall toward the interface. To further illustrate the transition of the flux-closure under the action of compressive stress, the out-of-plane lattice constant mapping of the transitional boundary region is depicted in *SI Appendix*, Fig. S6, which shows a sharp interface between the formed *a* domain and the flux-closure phase. The most salient feature in *SI Appendix*, Fig. S6*B* is that the large *a* domains close to the phase transition regions are significantly larger than those farther away, while the *c* domains are narrower, indicating gradual expansion of *a* domains and shrinkage of *c* domains during transition. Again, removal of the external stress leads to spontaneous recovery from *a* domains to the flux-closure structure. As shown in the sixth image of Fig. 4*H*, when the stress is reduced, the flux-closure structure is restored to its original position. The process of stress-induced flux-closure transition and recovery is confirmed by the continuously recorded selected area electron diffraction patterns (*SI Appendix*, Fig. S7) and dark-field images (*SI Appendix*, Fig. S8), respectively. The stress magnitude required to initiate phase transition is measured to be ~11 μN (see *Methods* for more details), as shown by the yellow star in Fig. 4*J*. Furthermore, the reversibility and repeatability are also demonstrated by the six cycles of switching–recovery shown in *SI Appendix*, Fig. S9.

Controllable and reversible manipulations of flux-closures by an electric field or a mechanical force, can be precisely reproduced by phase field simulations, as shown in Fig. 5*A* and *SI Appendix*, Fig. S10. Application of an electric field favors the *c* domain with polarization parallel to the electric field, leading to shrinkage of the unfavored *a* domain and *c* domain with polarization antiparallel to the electric field. The shrinkage of the unfavored *c* domain, resulting in the gradual motion of the two 90° domain walls on both sides, is accompanied by the gradual approach of the two flux-closure cores (since in this system the 90° domain walls are always rooted at the flux-closure core). Once the unfavored *c* domain has been erased, the 180° domain wall disappears and the flux-closure cores are broken, and the flux-closures change into *a*/*c* domain states. Therefore, the gradient energy drops at the flux-closure–*a*/*c* phase boundary, as shown in Fig. 5*B*. A further increase in the electric field rotates the electric dipoles of the *a* domain to align with the field and thus causes growth of the favored *c* domain with polarization parallel to the electric field and shrinkage of the *a* domain. Since there is no domain wall formation or elimination, the gradient energy remains almost constant in the *a*/*c* phase. Finally, when the applied voltage reaches 7 V, the *a* domains vanish completely and the *a*/*c* phase becomes a single *c* domain state, in which all the dipoles align themselves with the applied electric field. All domain walls disappear, and the gradient energy reaches its minimum. During the whole switching process, both 90°- and 180°-polarization switching can be induced by the external electric field.

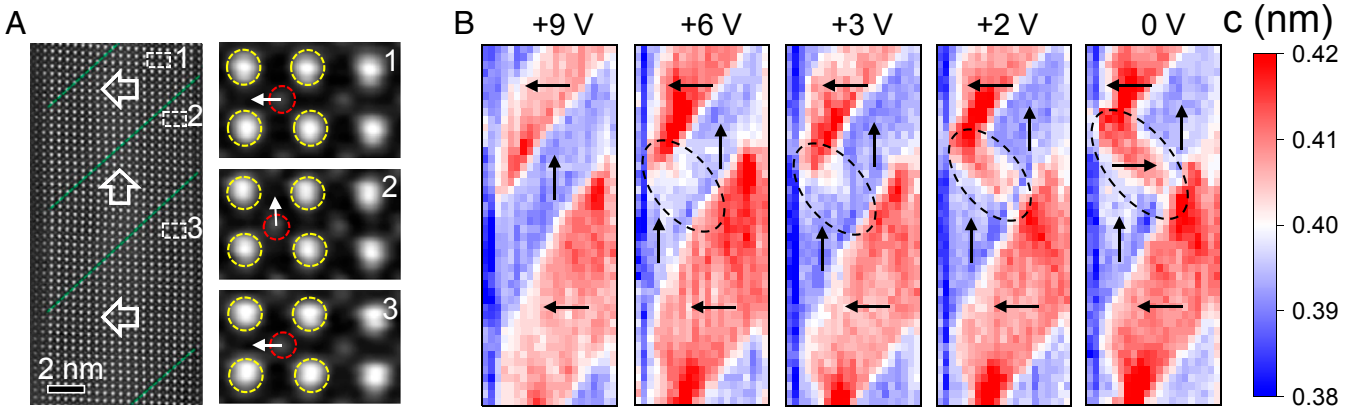

Fig. 3. Recovery of flux-closure. (*A*) Atomically resolved HAADF-STEM image showing the switched area with *a*/*c* domains. Enlarged HAADF-STEM images corresponding to the areas labeled 1, 2, and 3 on the left show the polarization direction of Ti with respect to Pb. The yellow and red circles indicate the positions of Pb and Ti columns, respectively. (*B*) Out-of-plane lattice constant mapping series corresponding to the HAADF-STEM images acquired during gradual removal of the electric field, showing the flux-closure recovery process. Thin black arrows indicate the spontaneous polarization direction of PTO. The dashed oval highlights the growth of the c^+ domain.

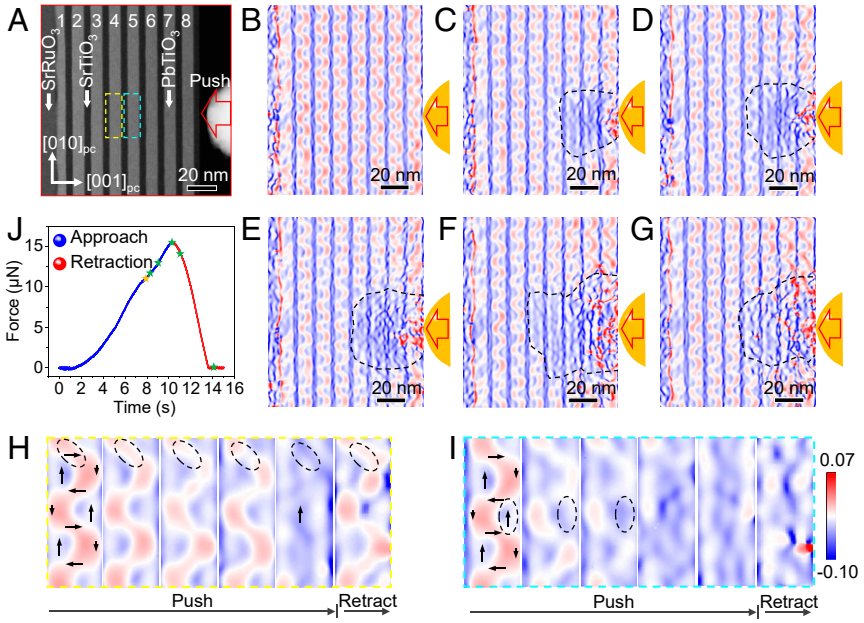

Fig. 4. Tracking the process of flux-closure transition under mechanical stress at the atomic scale. (*A*) HAADF-STEM image before mechanical stress loading. (*B*–*G*) Out-of-plane strain (ε_{yy}) maps extracted via the GPA analysis corresponding to the series of chronologically acquired HAADF-STEM images under different mechanical stresses. The black dashed lines highlight the boundary between the transformed and untransformed areas. (*H* and *I*) Enlarged GPA images corresponding to the representative areas outlined by yellow and cyan rectangles in *A* extracted from *B*–*G*. Black arrows indicate the spontaneous polarization direction of PTO. (*J*) Mechanical load versus time. The blue points represent the approach branch and the red points represent the retraction branch. The yellow star indicates the starting point of the phase transition, and the green stars correspond to the images in *SI Appendix*, Fig. S8*A*.

However, a compressive stress can lead to different motions of domain walls. With the application of compressive stress, the *c* domains shrink, whereas the *a* domains grow, as shown in Fig. 5*A*. Besides the motion of 90° domain walls, the shrinkage of *c* domains also leads to shortening of 180° domain walls and gradual motion of the flux-closure core toward the PTO/STO interface. The decrease in 180° domain walls with increasing stress results in a reduction in gradient energy in the flux-closure phase. When the applied force exceeds 8 μN, the 180° domain wall is fully erased, with elimination of the flux-closure core, leading to destruction of the flux-closure. Thus, the flux-closure transforms into an *a*/*c* phase. Further increase in stress will gradually eliminate the *c* domains, with the gradient energy continuing to decrease owing to the decrease in 90° domain walls on both sides of the *c* domain, as shown in Fig. 5*C*. When the applied force exceeds 10 μN, all the *c* domains disappear and the *a*/*c* phase switches into a single *a* domain state, where the gradient energy reaches its minimum with no domain walls left. In contrast to electrical control, a stress field can only induce 90°-polarization switching.

The phase field simulations not only precisely reproduce the experimentally observed evolution of flux-closure textures, but also reveal the underlying mechanism of domain evolution from an analysis of different energies. According to Ginzburg–Landau theory, the polarization-related energy is identical for *a* and *c* domains in the absence of an external field, which is the initial state of the flux-closure phase. As shown in Fig. 5*D*, an applied electric field can modify the energy profile, lowering the energy with polarization parallel to the electric field and raising the energy with polarization antiparallel to the electric field. Therefore, the electric field can drive the transformation of a flux-closure into a single *c* domain state with minimum energy. On the other hand, a compressive stress will decrease the energy of an *a* domain perpendicular to the stress direction and increase the energy of a *c* domain, as shown in Fig. 5*E*. Hence, under application of compressive stress, the *a* domain is preferred, and the flux-closure structure will switch into a single *a* domain.

Discussion

Since a flux-closure and a polar vortex have very different domain wall configurations, we now compare the observed switching dynamics of a polar flux-closure with previously reported results for a polar vortex. Phase-field simulations have demonstrated the possibility of switching polar vortices: under the application of an electrical field, vortex cores with opposite curls move closer until they reach the same lateral position and then produce new *a* domains, and the reverse process of back-switching takes place when the applied field is removed (37). The evolution of vortices driven by temperature change (29), electric field, and stress have been probed experimentally by X-ray diffraction, PFM (29), and TEM (30, 31). Damodaran et al. (29) found phase coexistence of vortex and ferroelectric phases and electric-field-driven interconversion between them. Du et al. (30) reported that vortices can split, transform to polar waves, and finally become a stable *c* domain that does not recover spontaneously. According to Chen et al. (31), under mechanical stress, a polar vortex can be switched to an *a* domain and reversibly recover after removal of stress. In our study, the switching behaviors of flux-closures are even more complicated than those of vortices, because the transformation of a flux-closure involves not only the topological core but also the ordinary ferroelectric 90° and 180° domain walls. Nevertheless, for both a polar vortex and a flux-closure, the external stimulus required for phase transition (either an electric field or a stress field) is comparable to that required to switch an ordinary domain (34, 38, 39), indicating their practicability for fabricating flux-closure-based nanoelectronics and electromechanical devices.

Finally, we should mention the advantages of atomically resolved in situ TEM/STEM in comparison with previous X-ray diffraction and PFM approaches (29): these include high spatial and temporal resolution, as well as access to structural

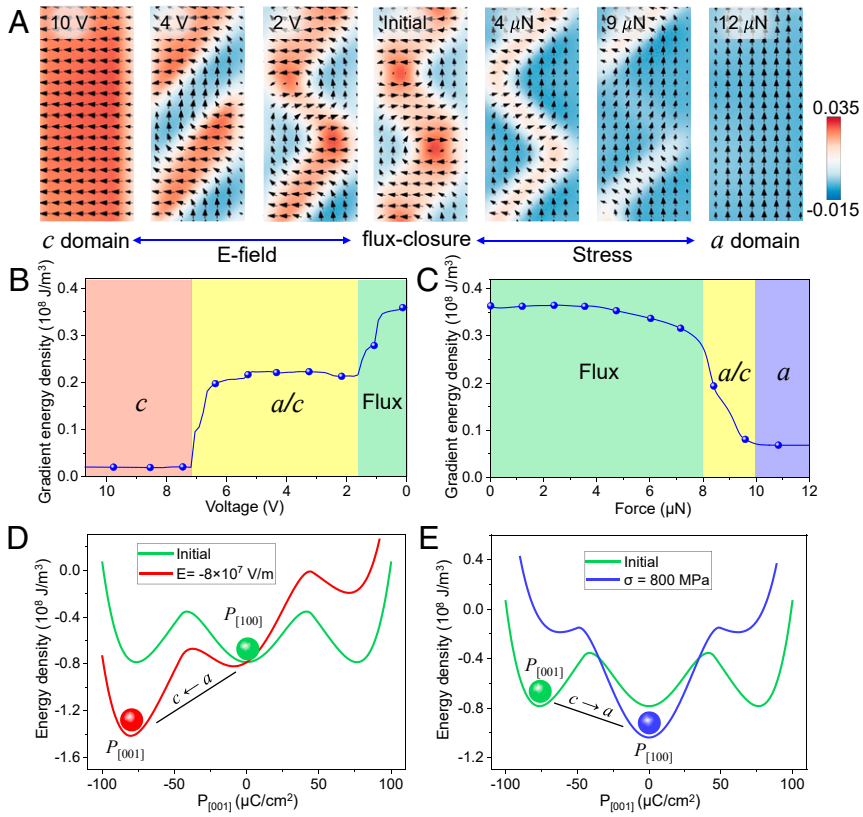

Fig. 5. Phase field simulation of flux-closure evolution. (*A*) Domain switching processes of a flux-closure under an electric field and under a mechanical load. The background colors denote different magnitudes of strain in the [001] direction corresponding to the out-of-plane strain (ε_{yy}) in GPA. (*B* and *C*) Phase diagrams of the domain structure in the PTO layer under an applied electric field and a mechanical load, respectively. The blue lines denote the gradient energy densities of PTO, which are used to determine the phase boundary. (*D* and *E*) Calculated polarization related energy profiles in the PTO layer. The green lines represent the energy profile in the flux-closure phase. The red and blue lines denote the energy profile under an applied electric field and a mechanical load, respectively.

information on buried interfaces, which allows the polarization evolution of individual topological polar structures to be tracked. Although local damage to the outermost surface is possible during in situ TEM, mainly due to contact with the rough surface of the probe, this should be avoidable in practical devices through the use of a thin surface protective layer or a fixed contact. However, it should also be noted that since these topological structures are formed as a result of delicate competition between different energies, the destructive process required for TEM sample preparation must be assumed to have some degree of influence on the boundary conditions. Nevertheless, the well-preserved flux-closure pattern in our cross-sectional TEM specimen, which is almost identical to that seen from other characterizations such as X-ray and PFM, suggests that the boundary conditions for the flux-closure are not significantly affected. Therefore, our observations from in situ TEM present the key features of the evolution of flux-closures under external stimuli, which have been confirmed by the phase field simulations.

Conclusion

In summary, the transition between a topological flux-closure and ordinary ferroelectric domains in $PbTiO_3/SrTiO_3$ superlattices has been controllably manipulated by the application of electrical and mechanical stimuli. A combination of atomically resolved in situ (S)TEM experiments and phase field simulations has enabled us to capture structural and physical details during the transition. Under electrical loading, the topological structure of the flux-closure gradually starts to break, and it is converted into intermediate *a*/*c* domains at ~23.7 MV/m. Eventually a single *c* domain can be obtained, the polarization direction of which depends on the external electric field. Under mechanical loading, the compressive stress (~11 μN) results in shrinkage of the *c* domain and expansion of the large *a* domain to form *a*/*c* domains through movement of the flux-closure core and elimination of 180° domain walls. With increasing stress, a single *a* domain can be obtained. These switching processes are completely reversible. During these phase transitions, the evolutions of competing energies are revealed by phase field simulations. The electric energy dominates the reduction of the total energy under an electric field, whereas the elastic energy plays the dominant role in energy reduction under application of mechanical force. The ability to reversibly manipulate topological polar structures and the controllable switching between them and ordinary ferroelectric domain structures provides a solid foundation for their application to nanoelectronics and electromechanical devices. Furthermore, although the final domain states are different under both stress and electric fields, the switching pathways share the same *a*/*c* intermediate domain state, indicating the superior stability of monodomain and *a*/*c* domain compared to topological flux-closure with external elastic and/or electrostatic energy being increasing. Generally, the engineering of boundary conditions via substrate strain and electrostatic state of interfacial electrode/insert/cap layers were used to create new polar structures. The in situ application of external stimuli with continuous magnitude appears to an alternative method to control the boundary conditions and thus can help us to search for more new topological polar structures that may only exist in a narrow window and unachievable from the regular thin film growth.

Methods

Thin Film Growth. Superlattice films of $[(PTO)_{19}/(STO)_{11}]_8$ were deposited on a $(110)_{pc}$–$GdScO_3$ substrate with an SRO-buffered layer in a pulsed laser deposition system (PVD-5000) equipped with a KrF excimer laser ($\lambda = 248$ nm). Ceramic targets of $SrRuO_3$, $Pb_{1.1}TiO_3$ (10 mol% excess lead to compensate for evaporation loss of Pb), and $SrTiO_3$ were used for the SRO layer and PTO/STO superlattice deposition. The SRO-buffered layer was first grown at 690 °C and 80-mTorr oxygen pressure, and then the substrate was cooled to 600 °C for deposition of the PTO/STO superlattice at 200-mTorr oxygen pressure. Selection of the appropriate laser energy was crucial for ensuring layer-by-layer growth of the SRO, PTO, and STO sublayers, and here the SRO and PTO/STO superlattices were prepared under laser energies of 390 and 350 mJ/pulse, respectively. By controlling the growth time, the thicknesses of the PTO and STO layers were held at 8 nm and 4.8 nm. Immediately after growth, the superlattice films were cooled to room temperature at a rate of 50 °C min^{-1}.

TEM Sample Preparation. Cross-sectional TEM samples were prepared by a conventional method involving mechanical polishing followed by ion-beam milling. The ion-beam milling was carried out using argon ions (Gatan 695) with an acceleration voltage of 2.6 kV, and decreased to 0.1 kV to reduce irradiation damage to the layers.

STEM Characterization. HAADF images for sample characterization were obtained using an aberration-corrected JEOL Grand ARM 300 CFEG and FEI Titan Cube Themis G2. The collection semiangle snap for the HAADF imaging ranged from 54 to 220 mrad (JEOL) and from 39 to 200 mrad (Titan).

Polarization Mapping. The position of each atom in the HAADF image was determined by simultaneously fitting with a 2D Gaussian peak to an a priori perovskite unit cell using a MATLAB code. The polarization distribution was then obtained (*SI Appendix*, Fig. S1).

In Situ (S)TEM. In situ (S)TEM experiments were carried out using an aberration-corrected JEOL ARM 300F at 300 kV in STEM and TEM modes. The real-time diffraction pattern, dark-field TEM images, and atomic HAADF-STEM images were recorded using a JEOL ARM 300F with a double-tilt holder provided by the ZEPTools Technology Company. The acquisition parameters of the real-time diffraction pattern were 4,096 × 4,096 pixels for each frame and 7 frames/s. The dark-field TEM images related to the applied electric field were completed in TEM mode with the microscope equipped with a OneView camera (Gatan). The images were recorded with 4,096 × 4,096 pixels for each frame and 25 frames/s; the corresponding temporal resolution was 0.04 s. Quantitative measurements of the mechanical loads were performed using an FEI F20 microscope operated at 200 kV in TEM mode and equipped with a OneView camera together with a Hysitron system (PI 95). The images were recorded with 1,024 × 1,024 pixels for each frame and 10 frames/s from the OneView camera; the corresponding time resolution was 0.1 s. The atomic HAADF-STEM images were recorded with 2048×2048 pixels for each frame, and the dwell time of each pixel was 4 μs.

Electric Field Calculations. The distribution of electrical fields in the PTO/STO superlattice was calculated using Ansoft Maxwell software based on finite element analysis and Maxwell's equations (39–41). For simplicity, all calculations assumed SRO and tungsten to be perfect conductors and the PTO/STO superlattice to be a perfect insulator. We estimated the tip contact width to be ∼20 nm. The relative dielectric constants of STO and PTO were assumed to be 300 and 200. The calculation model consisted of eight superlattice periods, in which the thicknesses of PTO and STO were estimated to be ∼8 nm and ∼4.8 nm, respectively. The in-plane and out-of-plane components of the electric field distribution were determined by calculating the electric potential distribution and its partial derivatives.

Phase Field Simulations. In the phase-field model, the free-energy density f derived for a $PbTiO_3/SrTiO_3$ superlattice thin film has the following form (42):

$$f = \alpha_i P_i^2 + \alpha_{ij} P_i^2 P_j^2 + \alpha_{ijk} P_i^2 P_j^2 P_k^2 + \frac{1}{2} c_{ijkl} \varepsilon_{ij} \varepsilon_{kl} - q_{ijkl} \varepsilon_{ij} P_k P_l + \frac{1}{2} g_{ijkl} P_{i,j} P_{k,l} - \frac{1}{2} \varepsilon_0 \varepsilon_r E_i E_i - E_i P_i, \quad [1]$$

where α_i, α_{ij}, and α_{ijk} are the Landau expansion coefficients (sixth- and fourth-order forms for PTO and STO, respectively), c_{ijkl} are the elastic constants, q_{ijkl} are the electrostrictive coefficients, g_{ijkl} are the gradient energy coefficients, ε_0 is the vacuum permittivity, ε_r is the relative dielectric constant of the background material (cubic PTO and STO in this case), and P_i, ε_{ij}, and E_i are the polarization, strain, and electric field components, respectively. The temporal evolution of the polarization field can be described by the time-dependent Ginzburg–Landau (TDGL) equation as follows:

$$\frac{\partial P_i(\boldsymbol{r}, t)}{\partial t} = -L \frac{\delta F}{\delta P_i(\boldsymbol{r}, t)}, \quad [2]$$

where L is the domain wall mobility; $F = \int_V f \, dV$ is the total free energy in the whole structure, and $\boldsymbol{r}$ and t are the spatial position vector and time, respectively. In addition, both the mechanical equilibrium equation

$$\sigma_{ij,j} = \frac{\partial}{\partial x_j} \left(\frac{\partial f}{\partial \varepsilon_{ij}} \right) = 0 \quad [3]$$

and Maxwell's equation

$$D_{i,i} = -\frac{\partial}{\partial x_i} \left(\frac{\partial f}{\partial E_i} \right) = 0, \quad [4]$$

need to be satisfied simultaneously for a body-force-free and charge-free ferroelectric system, in which σ_{ij} and D_i are the stress and electric displacement components, respectively. To solve the above equations, the nonlinear finite element method and backward Euler iteration method are employed for space discretization and time integration, respectively. 2D simulation along the [100]–[001] crystallographic plane is carried out for clearer illustration and computational simplicity. The thickness of the PTO and STO layers in the simulation are 8 nm and 4.8 nm, which are identical to those in the experimental set. Discrete grids with $\Delta x = \Delta z = 0.4$ nm in real space are used for space discretization, and the step length for time integration is chosen as $\Delta t / t_0 = 0.2$, where $t_0 = 1/(\alpha_0 L)$ and α_0 is the absolute value of α_1 at room temperature. Periodic boundary conditions for the electric potential and polarization components are employed along the x direction. The material parameters for PTO and STO used in the simulations are listed in *SI Appendix*, Table S1. In addition, the isotropic gradient energy coefficients for PTO and STO are both chosen as $g_{11}/G_{110} = 0.4$, where $G_{110} = 1.73 \times 10^{-10}$ C^{-2} m^4 N. A small random fluctuation (<$0.01P_0$, where $P_0 = 0.757$ C m^{-2} is the spontaneous polarization of PTO at room temperature) is used as the initial setup for polarization to initiate the simulation. In addition, the resulting interlayer mechanical inhomogeneity is considered in the modeling by exerting a misfit strain of −0.2% on the PTO layers.

Data Availability. All data, materials, and experimental procedures that support the findings of this study are available in the text, *Methods* and *SI Appendix*.

ACKNOWLEDGMENTS. This research was supported by the National Key R&D Program of China (Grants 2016YFA0300804 and 2016YFA0300903), the Program from Chinese Academy of Sciences (Grant ZDYZ2015-1 and XDB33030200), the National Natural Science Foundation of China (Grants 11974023, 51672007, 11875229, 51872251, 21773303, 51991344, and 51421002), the Key R&D Program of Guangdong Province (2018B030327001, 2018B010109009), the Bureau of Industry and Information Technology of Shenzhen (Grant 201901161512), and the "2011 Program" Peking–Tsinghua–IOP Collaborative Innovation Center for Quantum Matter.

1. P. Aguado-Puente, J. Junquera, Ferromagneticlike closure domains in ferroelectric ultrathin films: First-principles simulations. *Phys. Rev. Lett.* **100**, 177601 (2008).
2. J. F. Scott, Applications of modern ferroelectrics. *Science* **315**, 954–959 (2007).
3. N. Nagaosa, Y. Tokura, Topological properties and dynamics of magnetic skyrmions. *Nat. Nanotechnol.* **8**, 899–911 (2013).
4. H. Du *et al.*, Interaction of individual skyrmions in a nanostructured cubic chiral magnet. *Phys. Rev. Lett.* **120**, 197203 (2018).
5. N. S. Kiselev *et al.*, Chiral skyrmions in thin magnetic films: New objects for magnetic storage technologies? *J. Phys. D Appl. Phys.* **44**, 392001 (2011).
6. X. Zhang, M. Ezawa, Y. Zhou, Magnetic skyrmion logic gates: Conversion, duplication and merging of skyrmions. *Sci. Rep.* **5**, 9400 (2015).
7. A. Fert, V. Cros, J. Sampaio, Skyrmions on the track. *Nat. Nanotechnol.* **8**, 152–156 (2013).
8. K.-E. Kim *et al.*, Configurable topological textures in strain graded ferroelectric nanoplates. *Nat. Commun.* **9**, 403 (2018).
9. Y. L. Tang *et al.*, Observation of a periodic array of flux-closure quadrants in strained ferroelectric $PbTiO_3$ films. *Science* **348**, 547–551 (2015).
10. Y. Liu *et al.*, Large scale two-dimensional flux-closure domain arrays in oxide multilayers and their controlled growth. *Nano Lett.* **17**, 7258–7266 (2017).

11. J. Seidel *et al*., Topological structures in multiferroics - domain walls, skyrmions and vortices. *Adv. Electron. Mater.* **2**, 1500292 (2016).
12. A. K. Yadav *et al*., Observation of polar vortices in oxide superlattices. *Nature* **534**, 138 (2016).
13. Y. Ivry, D. P. Chu, J. F. Scott, C. Durkan, Flux closure vortexlike domain structures in ferroelectric thin films. *Phys. Rev. Lett.* **104**, 207602 (2010).
14. I. Naumov, H. Fu, Vortex-to-polarization phase transformation path in ferroelectric $Pb(ZrTi)O_3$ nanoparticles. *Phys. Rev. Lett.* **98**, 77603 (2007).
15. C. L. Jia, K. W. Urban, M. Alexe, D. Hesse, I. Vrejoiu, Direct observation of continuous electric dipole rotation in flux-closure domains in ferroelectric $Pb(Zr,Ti)O_3$. *Science* **331**, 1420–1423 (2011).
16. S. Li *et al*., Periodic arrays of flux-closure domains in ferroelectric thin films with oxide electrodes. *Appl. Phys. Lett.* **111**, 52901 (2017).
17. S. K. Streiffer *et al*., Observation of nanoscale 180° stripe domains in ferroelectric $PbTiO_3$ thin films. *Phys. Rev. Lett.* **89**, 67601 (2002).
18. I. Kornev, H. Fu, L. Bellaiche, Ultrathin films of ferroelectric solid solutions under a residual depolarizing field. *Phys. Rev. Lett.* **93**, 196104 (2004).
19. B. K. Lai *et al*., Electric-field-induced domain evolution in ferroelectric ultrathin films. *Phys. Rev. Lett.* **96**, 137602 (2006).
20. E. Bousquet *et al*., Improper ferroelectricity in perovskite oxide artificial superlattices. *Nature* **452**, 732–736 (2008).
21. D. Sichuga, L. Bellaiche, Epitaxial $Pb(Zr,Ti)O_3$ ultrathin films under open-circuit electrical boundary conditions. *Phys. Rev. Lett.* **106**, 196102 (2011).
22. S. Li *et al*., Evolution of flux-closure domain arrays in oxide multilayers with misfit strain. *Acta Mater.* **171**, 176–183 (2019).
23. I. I. Naumov, L. Bellaiche, H. Fu, Unusual phase transitions in ferroelectric nanodisks and nanorods. *Nature* **432**, 737–740 (2004).
24. L. V. Lich *et al*., Switching the chirality of a ferroelectric vortex in designed nanostructures by a homogeneous electric field. *Phys. Rev. B* **96**, 134119 (2017).
25. L. J. McGilly, A. Schilling, J. M. Gregg, Domain bundle boundaries in single crystal $BaTiO_3$ lamellae: Searching for naturally forming dipole flux-closure/quadrupole chains. *Nano Lett.* **10**, 4200–4205 (2010).
26. L. J. McGilly, J. M. Gregg, Polarization closure in $PbZr_{0.42}Ti_{0.58}O_3$ nanodots. *Nano Lett.* **11**, 4490–4495 (2011).
27. R. G. P. McQuaid, A. Gruverman, J. F. Scott, J. M. Gregg, Exploring vertex interactions in ferroelectric flux-closure domains. *Nano Lett.* **14**, 4230–4237 (2014).
28. L. W. Chang, V. Nagarajan, J. F. Scott, J. M. Gregg, Self-similar nested flux closure structures in a tetragonal ferroelectric. *Nano Lett.* **13**, 2553–2557 (2013).
29. A. R. Damodaran *et al*., Phase coexistence and electric-field control of toroidal order in oxide superlattices. *Nat. Mater.* **16**, 1003–1009 (2017).
30. K. Du *et al*., Manipulating topological transformations of polar structures through real-time observation of the dynamic polarization evolution. *Nat. Commun.* **10**, 4864 (2019).
31. P. Chen *et al*., Atomic imaging of mechanically induced topological transition of ferroelectric vortices. *Nat. Commun.* **11**, 1840 (2020).
32. G. Catalan *et al*., Flexoelectric rotation of polarization in ferroelectric thin films. *Nat. Mater.* **10**, 963–967 (2011).
33. B. Warot-Fonrose *et al*., Mapping inelastic intensities in diffraction patterns of magnetic samples using the energy spectrum imaging technique. *Ultramicroscopy* **108**, 393–398 (2008).
34. P. Gao *et al*., Atomic-scale mechanisms of ferroelastic domain-wall-mediated ferroelectric switching. *Nat. Commun.* **4**, 2791 (2013).
35. C. L. Jia *et al*., Unit-cell scale mapping of ferroelectricity and tetragonality in epitaxial ultrathin ferroelectric films. *Nat. Mater.* **6**, 64–69 (2007).
36. P. Gao *et al*., Possible absence of critical thickness and size effect in ultrathin perovskite ferroelectric films. *Nat. Commun.* **8**, 15549 (2017).
37. Z. J. Hong, L. Q. Chen, Blowing polar skyrmion bubbles in oxide superlattices. *Acta Mater.* **152**, 155–161 (2018).
38. P. Gao *et al*., Ferroelastic domain switching dynamics under electrical and mechanical excitations. *Nat. Commun.* **5**, 3801 (2014).
39. P. Gao *et al*., Revealing the role of defects in ferroelectric switching with atomic resolution. *Nat. Commun.* **2**, 591 (2011).
40. P. Gao *et al*., Direct observations of retention failure in ferroelectric memories. *Adv. Mater.* **24**, 1106–1110 (2012).
41. C. T. Nelson *et al*., Domain dynamics during ferroelectric switching. *Science* **334**, 968–971 (2011).
42. J. Wang *et al*., Role of grain orientation distribution in the ferroelectric and ferroelastic domain switching of ferroelectric polycrystals. *Acta Mater.* **61**, 6037–6049 (2013).